Study of the Reaction of Hydroxylamine with Iridium Atomic and Cluster Anions (*n* = 1−5)

Published as part of The Journal of Physical Chemistry virtual special issue "Alexander Boldyrev Festschrift".

Sandra M. Ciborowski, Robert Buszek, Gaoxiang Liu, Moritz Blankenhorn, Zhaoguo Zhu,
Mary A. Marshall, Rachel M. Harris, Tatsuya Chiba, Evan L. Collins, Sara Marquez, Jerry A. Boatz,*
Steven D. Chambreau,* Ghanshyam L. Vaghjiani, and Kit H. Bowen*

ACCESS | Metrics & More | Article Recommendations | Supporting Information

ABSTRACT: Elucidating the multifaceted processes of molecular activation and subsequent reactions gives a fundamental view into the development of iridium catalysts as they apply to fuels and propellants, for example, for spacecraft thrusters. Hydroxylamine, a component of the well-known hydroxylammonium nitrate (HAN) ionic liquid, is a safer alternative and mimics the chemistry and performance standards of hydrazine. The activation of hydroxylamine by anionic iridium clusters, Ir_n^- ($n = 1-5$), depicts a part of the mechanism, where two hydrogen atoms are removed, likely as H_2, and $Ir_n(NOH)^-$ clusters remain. The significant photoelectron spectral differences between these products and the bare clusters illustrate the substantial electronic changes imposed by the hydroxylamine fragment on the iridium clusters. In combination with DFT calculations, a preliminary reaction mechanism is proposed, identifying the possible intermediate steps leading to the formation of $Ir(NOH)^-$.
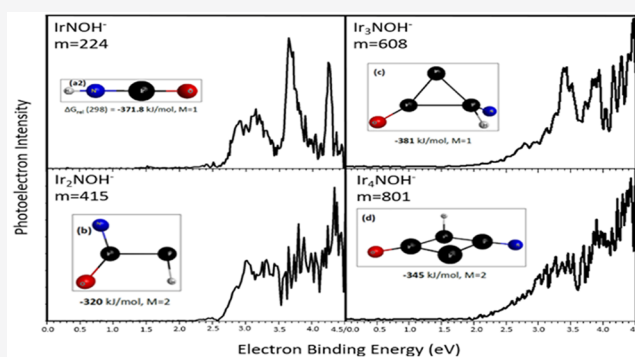
1. INTRODUCTION

Since the 1960s, the most often used propellants for spacecraft thrusters are composed of hydrazine (N_2H_4) and its derivatives. Although hydrazine is effective as a monopropellant, efforts are underway to find a substitute for hydrazine compounds due to their significant hazards. Ionic liquids have been proposed as a potential alternative due to their safer properties such as negligible vapor pressure and comparable performance as a propellant. The ability to model the performance of propulsion systems depends on a fundamental knowledge of the physical and chemical processes involved in ignition and combustion.

Liquid propellants based on nitrogen-containing compounds, including hydroxylammonium nitrate (HAN) and other ionic liquids, have shown promise in terms of effectiveness and safety.[1−6] These ionic liquids also cross the boundary between monopropellants and possible use as multimode propellants, which are especially promising for high-efficiency electrospray thrusters and high-performance catalyzed (chemical) thrusters.[7] Hydroxylammonium nitrate (HAN) was first proposed for use as a rocket propellant in the 1990s.[1] More recently, HAN-based ionic liquid (IL) formulations have been proposed to replace hydrazine as a monopropellant[2−5] and for use in electric propulsion

applications.[6] The numerous benefits of using HAN-based ILs over hydrazine include, for example, the reduced toxicity and respiratory hazards, higher stability with reduced explosion hazards for long-term storage, and increased performance. HAN has not been shown to be carcinogenic or mutagenic[1] and has a very low vapor pressure, whereas hydrazine has a significant vapor pressure and requires a S.C.A.P.E. apparatus for handling.[4] HAN has a low freezing point and high density, potentially enabling an increase in density specific impulse (d-Isp)[4] with its use as a monopropellant. HAN formulations have been successfully implemented in SDS-4 (JAXA) and AF-M315E (AFRL/NASA GPIM) fueled satellites.[8] Additionally, the use of HAN in electrical propulsion applications has attracted much interest recently in the potential use in high-efficiency microthrusters.[6] In a laboratory environment, these ionic liquids can be safer to handle and are capable of

mimicking the reactivity observed between catalysts and hydrazine fuels.[1,4,6,8]

Much work has been done on the thermal decomposition and combustion mechanisms of HAN,[9−11] but there is not a real consensus on these mechanisms due to the variety in experimental and theoretical approaches and conditions applied thus far. More importantly, the mechanism for the heterogeneous catalysis of HAN is largely unknown, and this is the focus of this work. As a protic ionic liquid, the generally accepted first step in its decomposition is the proton transfer from the hydroxylammonium cation to the nitrate anion, producing hydroxylamine (HA) and HNO_3 neutral molecules. It has been proposed that the ignition of HAN-based formulations is initiated by proton transfer leading to formation of HNO_3 and nitrogen oxides that can subsequently react with the fuel species to ignite.[5] This is consistent with a recent publication indicating the formation of NO and HNO_3 upon contact of HAN with a hot Ir catalyst.[8] HA (50% in H_2O) has been observed to decompose completely at 45−50 °C on an iridium catalyst, but no mechanism was proposed in that work.[12]

In general, iridium activation of small molecules has been used successfully in Air Force applications for fuels and propellants.[13−20] Thin coatings of iridium and its oxide make for durable engine ignition devices, for rocket combustion chambers, and as a component of anodes for oxidation or splitting of methanol, ammonia, acetic acid, and water, for example, in the oxygen evolution reaction.[14−20] Hydrazine decomposition is also facilitated with the use of an iridium catalyst,[21] and this mechanism has been well studied. The use of an iridium catalyst significantly improves the efficiency of achieving activation in hydrazine, decreasing the initiation barrier from 65 to <10 kcal/mol.[22] This initiation comes in the way of breaking the N—N bond to create NH_2 radicals, enabling the decomposition to N_2, H_2, and NH_3.

Mass spectral and photoelectron studies show that single atomic species and small ionic clusters often cause this activation, for example, the breaking of O−H bonds in water, breaking a C−H bond in methane, and altering the bond angle in carbon dioxide. These small atoms and ionic clusters can be viewed as reasonable approximations of active sites in the bulk material and as fundamental starting points to assess catalytic reactivity.[23−36] Investigating the reactivity of highly uncoordinated small Ir_n^- clusters will lead to better understanding of reactive sites/reactivity at defects on bulk metal surfaces, although this study will not necessarily capture all ligands that are present on the bulk metal catalyst surface. Traditionally, studies performed by flowing the reactant gas over a premade surface of the catalyst or freezing the reactant gas and interacting the catalyst with its surface allow the observation of products formed from the catalysis of the small molecule, but these are complicated and expensive for current calculation methods. By focusing on isolated ionic atoms and clusters in the gas phase, individual steps and, in some cases, discernible products allow more specific details of the catalytic mechanism to be ascertained. These basic details allow for further understanding of the active sites of catalysts and provide benchmarks for contemporary calculations.

The catalytic properties of iridium have generated considerable interest in understanding the fundamental properties of iridium clusters, their interactions with other compounds and substrates, and the underlying chemistry of catalysis. Prior theoretical studies include investigations of the

structures, growth patterns, and properties of bare iridium clusters[37−40] and characterization of the low-lying excited states of $Ir_{2−8}$ clusters.[41] In addition, the fundamental interactions of iridium clusters with atomic[42,43] and molecular[44,45] hydrogen have been calculated. Several theoretical studies have probed the catalytic properties of iridium clusters, including correlation of catalytic activity with the cluster HOMO−LUMO gaps,[46] interactions with O_2, CO, and NO,[47] and dehydrogenation of ethane.[48] Incorporation of iridium clusters onto alumina and magnesium oxide substrates[49] has been studied by using density functional theory (DFT), including their catalytic effects on ethylene hydrogenation.[50] Schmidt et al.[22] used second-order perturbation theory and coupled-cluster theoretical methods to compare the decomposition of hydrazine in the gas phase to the catalyzed decomposition by Ir_4 and Ir_6 clusters supported on an alumina substrate. DFT investigations of iridium clusters on zeolite substrates[51] and their effects on hydrogen adsorption[52−54] and migration[55−57] also have been completed.

More recently, Koyasu et al.[58] conducted a combined experimental and theoretical study of the photoelectron spectroscopy (PES) of a series of anionic iridium clusters and their structural growth patterns. In addition, Lu et al.[59] refined the experimental electron affinity of atomic iridium,[60] and in a complementary follow-up theoretical paper by Barysz and Syrocki,[61] relativistic quantum chemical calculations were used to predict the photoelectron spectra of neutral iridium atom and its anion, including reassignment of some excited state levels.

To elucidate the heterogeneous catalysis mechanism, a combination of experimental and theoretical approaches are used here. Specifically, the reaction of the HA neutral with size-selected Ir_n^- ($n = 1−5$) anionic clusters is probed by using photoelectron spectroscopy (PES), and quantum chemical density functional theory (DFT) is used to model the potential energy surface(s) involved. Reaction R1 is proposed based on the species as detected by mass spectrometry (Figure 1).

$$HA + Ir_n^-(n = 1-5) \rightarrow Ir_nO^-(n = 1-5) + Ir_n(NOH)^-(n = 1-5) \tag{R1}$$
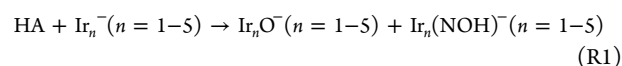
Observed mass spectrometric products guide the DFT effort. A size selection of each $Ir_n(NOH)^-$ ($n = 1−5$) cluster is then
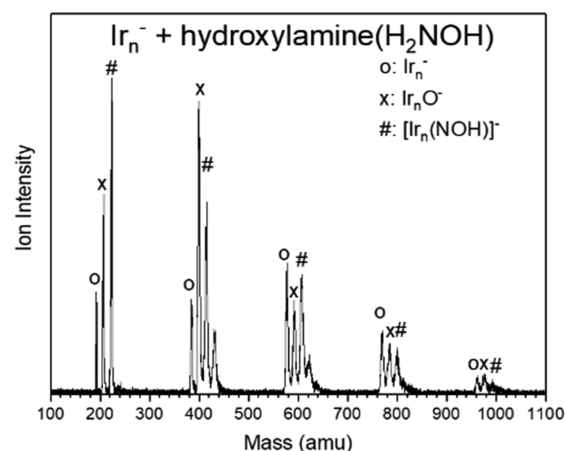
Figure 1. Mass spectrum of the interaction of laser-ablated anionic iridium clusters, Ir_n^-, with helium seeded with hydroxylamine (H_2NOH), resulting in a variety of Ir_n^-, Ir_nO^-, and $Ir_n(NOH)^-$ clusters, indicated by o, x, and #, respectively.

performed; the electron is photodetached by 266 nm photons, and the energy distributions of the electrons are measured (Figure 2). Photodetachment thresholds and higher energy
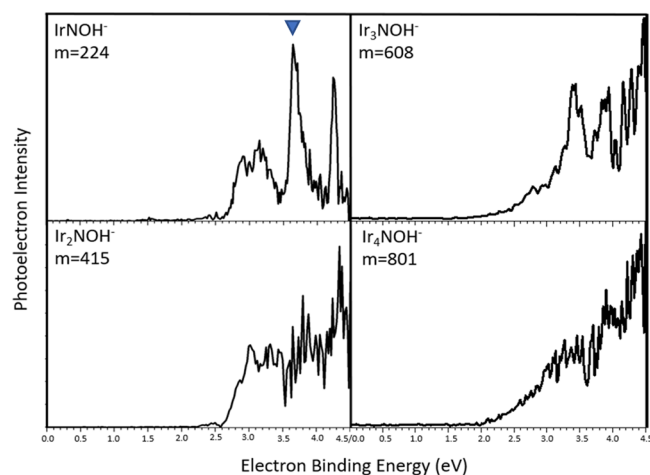
Figure 2. Photoelectron spectra of the $Ir_n(NOH)^-$ clusters ($n = 1-4$) taken with the fourth harmonic of the Nd:YAG laser (266 nm, 4.66 eV). The marked peak in the $Ir(NOH)^-$ spectrum comes from IrO_2^-.

features in the PES spectra give insight into the structure of the products. The combination of determining the atomic formulas for the products from the mass spectrometer, determining possible lowest-energy structures and their vertical electron detachment thresholds from DFT calculations, and computing the barriers involved on the potential energy surfaces will yield significant insight into the reaction of HA + Ir_n^- ($n = 1-5$) that is directly applicable to the heterogeneous catalysis process involved in HAN ignition on an iridium catalyst.

2. METHODS

2.1. Experimental Details. Anion photoelectron spectroscopy is conducted by crossing a mass-selected beam of negative ions with a fixed-frequency photon beam and energy-analyzing the resultant photodetached electrons. The photodetachment process is governed by the energy-conserving relationship: $h\nu = EBE + EKE$, where $h\nu$ is the photon energy, EBE is the electron binding (photodetachment transition) energy, and EKE is the electron kinetic energy. Our apparatus consists of a laser vaporization cluster anion source, a time-of-flight mass spectrometer, a Nd:YAG photodetachment laser, and a magnetic bottle energy analyzer.[62] The magnetic bottle photoelectron spectrometer resolution is ~35 meV at EKE = 1 eV. The fourth harmonic of a Nd:YAG laser (266 nm, 4.66 eV) was used to photodetach electrons from mass-selected cluster iridium–NOH anions, that is, $Ir_n(NOH)^-$ ($n = 1-5$). The well-known atomic transitions of Cu^- were used to calibrate the photoelectron spectra.[63]

The atomic and cluster anions of iridium were generated in a laser vaporization source. This source consisted of a rotating and translating iridium rod in a closed housing that was ablated with the focused second harmonic of a Nd:YAG laser (532 nm, 2.33 eV). After exiting the nozzle of the housing, the beam of iridium particles was crossed with a helium and hydroxylamine beam inside of a reaction cell. The generated ions were then sent through a skimmer and extracted into the time-of-flight mass spectrometer. Ions of interest were mass selected and

directed into the interaction region, where electrons were photodetached with the fourth harmonic of a Nd:YAG laser (266 nm, 4.66 eV), and photoelectron spectra were recorded.

2.2. Theoretical Details. The structures and relative energies of several isomers and electronic spin states of $Ir_n(NOH)^-$ ($n = 1-5$) were calculated by using density functional theory (DFT) methods, with the objective of identifying the most stable species, for which the electronic vertical detachment energies (VDEs) were subsequently computed. In addition, portions of the $Ir^- + NH_2OH$ potential energy surface were mapped to identify plausible mechanisms of formation of the most stable $Ir(NOH)^-$ species. The $\omega B97x$-d[64,65] range-separated functional, which includes dispersion corrections, in combination with the def2-TZVPPD basis set[66,67] for all atoms and the Stuttgart quasi-relativistic pseudopotential[68] for iridium were used.[69-72] This pairing of functional and basis set, hereafter denoted simply as $\omega B97x$-d/def2, was selected in part since the ground state electronic configuration of atomic iridium in the neutral ($[core]5s^2 5p^6 5d^7 6s^2$) and anionic ($[core]5s^2 5p^6 5d^8 6s^2$) states are correctly predicted at this level of theory. Furthermore, the $\omega B97x$-d/def2 predicted electron affinity of 1.50 eV is in excellent agreement with the experimental value of 1.564 eV,[59,60] lending additional confidence to the reliability of the calculated data. All structures were fully optimized and confirmed as local minima or first-order transition states via diagonalization of the mass-weighted matrix of energy second derivatives with respect to nuclear coordinates, that is, the Hessian matrix. The minimum-energy pathways connecting each transition state to reactants and products were traced by using intrinsic reaction coordinate (IRC) methods.[73,74] Relative Gibbs free energies at 298.15 K were calculated at all stationary points, with thermal and entropic corrections obtained from standard rigid-rotor, harmonic oscillator approximations,[75] by using harmonic vibrational frequencies scaled by a factor of 0.975.[76] Restricted and unrestricted DFT calculations were performed for closed- and open-shell systems, respectively.

The relative Gibbs free energies were used in exploring the $Ir^- + NH_2OH$ potential energy surface and to identify the most stable isomers and spin states of the $Ir_n(NOH)^-$ ($n = 1-5$) species. In contrast, vertical detachment energies of the latter were obtained by taking the difference in electronic energies between the anionic species and the corresponding neutral with the most stable spin state at the structure of the anion.

An additional set of calculations, with the CAMQTP01 range-separated functional[77] used in place of $\omega B97x$-d, were performed to probe the electronic transition energies between the anionic and neutral forms of $Ir_n(NOH)^-$ ($n = 1, 5$). The CAMQTP01 functional has been shown to predict accurate vertical ionization and excitation energies.[77] Optimized structures of the $Ir_n(NOH)^-$ ($n = 1, 5$) anion and neutral species were computed by using the difference in unscaled zero point energy-corrected total electronic energies to obtain adiabatic detachment energies (ADEs). In addition, VDEs were recomputed at the CAMQPT01/def2-TZVPP level using the procedure described previously. Finally, vertical excitation energies from the optimized neutral species were computed using time-dependent density functional theory (TDDFT). All calculations were performed using the GAMESS quantum chemistry program.[78,79]

3. RESULTS AND DISCUSSION

3.1. Photoelectron Spectra of Ir$_n$(NOH)$^-$. The mass spectrum presented in Figure 1 resulted from the interaction of HA with the anionic iridium clusters. No intact HA molecules were observed in conjunction with the Ir$_n^-$ clusters. Instead, the HA lost two hydrogen atoms, forming Ir$_n$(NOH)$^-$ cluster anions, as shown in reaction R1. Iridium oxide clusters, Ir$_n$O$^-$, were also present, resulting from the interaction with either HA or oxides present on the surface of the iridium rod. To eliminate the possibility that these peaks were actually due to mass-coincident Ir$_n$(NH$_2$)$^-$ produced during the reaction, photoelectron spectra for the species 16 amu heavier than the iridium clusters were taken, in both the presence and absence of HAN in the reaction cell (see Figures S1 and S2 in the Supporting Information). No differences in the spectra were observed, indicating no Ir$_n$(NH$_2$)$^-$ formation.

Photoelectron spectra of the Ir$_n$(NOH)$^-$ clusters ($n = 1-4$) are presented in Figure 2. The timing of the mass gate associated with the most intense signal for the Ir$_n$(NOH)$^-$ ($n = 1, 2$) species also apportioned small intensities of Ir$_n$O$_2^-$ species, both then entering the interaction region during photodetachment. To differentiate between the spectra of Ir(NOH)$^-$/Ir$_2$(NOH)$^-$ and the spectra of the corresponding Ir$_n$O$_2^-$ species, the photoelectron spectra were taken without the introduction of HA into the reaction cell and compared to the spectra obtained with HA. For $n = 1$, a single peak of the combined spectrum was clearly from the dioxide: this peak was marked with a blue triangle in the spectrum (see Figure 2 and Figure S3). The other peaks were substantially different from the dioxide and were clearly due to the Ir(NOH)$^-$ species. For $n = 2$, both spectra were normalized to the VDE peak of Ir$_2$O$_2^-$. The Ir$_2$O$_2^-$ spectrum was then subtracted from the spectrum taken in the presence of HA, producing the Ir$_2$(NOH)$^-$ spectrum presented in Figure 2 (see Figure S4). It is also important to note that all spectra are substantially different from spectra of their corresponding bare iridium clusters (see Figure S6).

Only Ir(NOH)$^-$ shows distinguishably separated peaks, (at 2.9, 3.15, and 4.25 eV) in its spectrum. Ir$_2$(NOH)$^-$ starts at 2.5 eV and displays three peaks in the feature between 2.5 and 3.5 eV. The onset energy of the two species Ir$_3$(NOH)$^-$ and Ir$_4$(NOH)$^-$ is ~2.0 eV. Two relatively sharp peaks are observed, centered around 3.4 and 3.9 eV, in the photoelectron spectrum of Ir$_3$(NOH)$^-$, while a series of peaks are seen between 3.0 and 3.5 eV in the spectrum of Ir$_4$(NOH)$^-$.

Although it is difficult to determine experimentally if the strongest peak in a feature corresponds to the vertical detachment energy (VDE) or the adiabatic detachment energy(ADE),[80] we refer to these features as VDEs, which arise from the transition between the anionic state and the neutral cluster state with the largest Franck–Condon overlap. Comparison of the calculated ADEs and VDEs with the observed values, summarized in Table 1, shows that the theoretical VDEs are in better agreement with experiment than the ADEs, with the exception of Ir(NOH)$^-$, for which the theoretical VDE and ADE are essentially the same. This suggests that the measured values correspond to VDEs. The comparison of the calculated VDE values and the measured values, shown in Table 1, support the assertion that the species seen in the mass spectrum are in fact Ir$_n$(NOH)$^-$ clusters, agreeing with the predominant reaction shown in reaction R1. Additionally, the measured VDE values for Ir$_n$(NOH)$^-$ are

**Table 1. Measured VDEs and Predicted VDEs and ADEs of Ir$_n$(NOH)$^-$ (in eV)**

species	measd VDE	theor VDE	theor ADE
IrNOH$^-$	2.90	2.96 (a2); 3.71 (a1)^a	2.94 (a2); 3.47 (a1)^a
Ir$_2$NOH$^-$	3.02	3.04	2.97
Ir$_3$NOH$^-$	3.39	3.34	3.20
Ir$_4$NOH$^-$	3.46	3.47	3.19
Ir$_5$NOH$^-$	3.3^b	3.32(e1); 3.32(e2); 3.41(e3)^a	3.15(e1); 3.14(e2); 3.10(e3)^a
IrO$_2^-$	3.64	3.48	3.44
Ir$_2$O$_2^-$	2.63	2.81	2.19

^{a}See Discussion section and Figure 3. ^{b}See Figure S5.

significantly different than their respective bare anionic clusters. For $n = 1$ to $n = 3$, the difference in the VDE between Ir$_n$(NOH)$^-$ and Ir$_n^-$ is >1 eV, and for the two largest clusters, $n = 4$ and 5, it is >0.8 eV. Large differences in the binding energy for ion–molecule interactions, as observed here, in addition to the fact that no Ir$_n$(NH$_2$OH)$^-$ was found in the mass spectrum, indicate that the interaction between the iridium clusters and hydroxylamine molecules is more than simple physisorption.

3.2. Theoretical Structures of Ir$_n^-$. The initial set of calculations focused on identifying the most stable isomers and electronic spin states of the anionic Ir$_n^-$ ($n = 1-5$) clusters, guided by the anionic cluster calculations by Koyasu et al.[58] as well as the corresponding neutral Ir$_n$ cluster calculations by Chen et al.[41] These two studies and others[37−40] illustrate the intrinsic challenges in theoretical characterizations of small iridium clusters due to complicating factors such as the presence of several low-lying excited states, significant multiconfigurational character, large spin–orbit interactions and relativistic effects, and so on. Consequently, the calculations presented here should not be regarded as definitive in nature but nonetheless of sufficient reliability to provide useful insights into the observed Ir$^-$ + NH$_2$OH chemistry and Ir(NOH)$^-$ photoelectron excitation energies.

The structures and spin multiplicities of the most stable Ir$_n^-$ ($n = 1-5$) isomers are summarized in Figure S7. The atomic iridium anion has a triplet ground state and 5d^{8}6s^2 valence configuration, in agreement with experiment.[59] The ground state of the diatomic anion is a sextet, with the octet, quartet, and doublet states higher in energy by 2.29, 0.33, and 0.65 eV, respectively. In comparison, Chen et al.[41] report a $^5\Delta_g$ ground state for the neutral diatomic at CCSD(T) and MRCI levels of theory. For the $n = 3$ anion, the predicted ground state is a symmetric D_{3h} ring with a multiplicity of 9. This is in contrast to the results of Koyasu et al.,[58] which predict a bent (C_{2v}) isomer with a spin multiplicity of 7. However, the present calculations predict a nonsymmetric ring isomer, also with a spin multiplicity of 7, which is only 0.17 eV above the D_{3h}, multiplicity = 9 ground state. The most stable Ir$_3^-$ linear $D_{\infty h}$ isomer found is a triplet, 0.69 eV above the ground state, whereas for neutral Ir$_3$, Chen et al.[41] report a linear $^2\Delta_g$ ground state. The $n = 4$ anion has a slightly distorted planar D_{4h} structure with spin multiplicity of 8, in agreement with the predicted structure and spin multiplicity by Koyasu et al.[58] Less stable $n = 4$ isomers include a planar C_{2v} [Ir$_3$−Ir]$^-$ and a tetrahedral cage structure, both with spin multiplicity of 8 and relative energies of 1.0 and 9.1 eV, respectively. For the $n = 5$ anion, multiple cage structures and spin multiplicities from 1 to
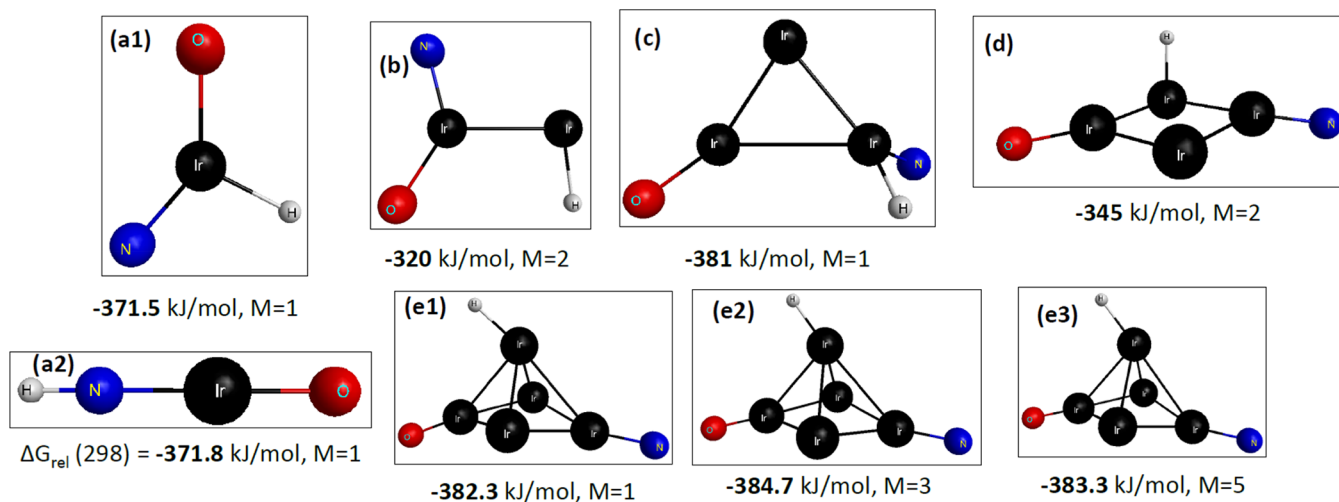
Figure 3. Lowest energy isomers of $Ir_n(NOH)^-$ ($n = 1-5$). Free energies are at 298.15 K, relative to separated $Ir_n^- + NH_2OH - H_2$, i.e., ΔG for the reaction $(Ir_n^- + NH_2OH \rightarrow Ir_n(NOH)^- + H_2)$. M denotes the spin multiplicity.

15 were explored. The most stable isomer found has a distorted square-pyramidal structure with spin multiplicity of 13, in agreement with Koyasu et al.

3.3. Theoretical Structures of $Ir_n(NOH)^-$. The next set of calculations focused on identifying the most stable isomers of $Ir_n(NOH)^-$, beginning with $n = 1$. The isomers considered for $n = 1$ included the unfragmented molecules $HN=O$ (bonded to Ir by either the N or O atom) and $N-OH$, plus all possible combinations of N,H,O fragments, that is, $N + OH$, $NH + O$, $NO + H$, and $N + O + H$, directly bonded to Ir^-, for a total of seven types of structural isomers. For each isomer, spin multiplicities of 1, 3, and 5 were considered. In the following, the notation $Ir_n(NOH)^-$ indicates the general, structural nonspecific complex, whereas individual isomer structures are qualitatively described by using the notation $Ir(a)(b)^-$ to indicate that moieties "a" and "b" are directly bonded to Ir but otherwise remain intact. For example, $Ir(O)(NH)^-$ denotes an isomer such as $O-Ir-NH^-$.

The optimized structures of the two most stable isomers, $Ir(O)(N)(H)^-$ and $Ir(O)(NH)^-$, which have nearly equal relative free energies, are shown in Figures 3a1 and 3a2, respectively. Additional less stable isomers are shown in Figure S8. The isomers in Figures 3a1 and 3a2 have a closed-shell singlet ground state. The least stable isomers have unfragmented $HN=O$ or $N-OH$ moieties (see Figure S8), with the partially fragmented isomers $Ir(NO)(H)^-$ and $Ir(N)(OH)^-$ having intermediate stabilities.

A similar computational sampling of representative isomers of $Ir_2(NOH)^-$ was completed, taking into account the possibility of fragments attaching to either a common Ir atom or to separate Ir atoms. In addition, spin multiplicities of 2, 4, and 6 were considered. The most stable isomer found was a fully fragmented spin-doublet $Ir_2(N)(O)(H)^-$ species in which the O and N atoms are bonded to a common Ir atom, as shown in Figure 3b. Additional isomers and the corresponding relative free energies are illustrated in Figure S9, all of which are doublets except for three spin-quartet isomers. As in the case of the $n = 1$ isomers, it is generally observed that Ir_2-HNO^- structures with an unfragmented HNO or ONH ligand are the least stable, and partially fragmented isomers such as $Ir_2(NO)(H)^-$ and $Ir_2(O)(NH)^-$ have intermediate relative energies.

For Ir_3-NOH^-, a more limited sampling of representative isomers was conducted. In particular, only the cyclic form of the Ir_3^- was considered, although an extended set of spin multiplicities ranging from 1 to 9 were calculated. The most stable isomer found was a fully fragmented spin singlet $Ir_3(N)(O)(H)^-$ structure in which the N and H atoms are bound to a common Ir, as illustrated in Figure 3c. As in the $n = 1$ and $n = 2$ cases, the stabilities of the $Ir_3(NOH)^-$ isomers generally increase with degree of HNO fragmentation, indicating that Ir–O, Ir–N, and Ir–H bonds are likely stronger than N–O, N–H, and O–H bonds. A representative subset of other isomers is shown in Figure S10. As an aside, an isomer with a bridging H atom was found (with a relative free energy of -271.1 kJ/mol), and a nitrogen atom was found to insert into an Ir–Ir bond (relative free energy of -354.3 kJ/mol), reflecting the greater number of configurational degrees of freedom associated with larger Ir_n^- clusters and possible weakening of the average Ir–Ir bond strength with increasing n.

Because the trends in relative isomer stability for $n = 1-3$ discussed above indicate an energetic preference for fragmented HNO, exploration of possible isomers for the $n = 4$ species was limited to partially and fully fragmented $Ir_4(NOH)^-$ species and further restricted to the planar arrangement of Ir_4^-. Spin multiplicities of 2, 4, 6, 8, and 10 were examined. The most stable isomer located is the doublet $Ir_4(N)(O)(H)^-$ structure shown in Figure 3d, in which each N, O, and H atom is bonded to a separate Ir atom. Additional representative isomers are shown in Figure S11, which include instances of a bridging N atom.

Consideration of potential isomers of Ir_5-NOH^- was restricted to the square-pyramidal form of Ir_5^- and only the $Ir_5(NH)(O)^-$ and $Ir_5(N)(O)(H)^-$ fragmented species. Spin multiplicities of 1–13 were considered because of the predicted ground state multiplicity of 13 for the bare Ir_5^- anion. The most stable isomer found was the $Ir_5(N)(O)(H)^-$ triplet state structure shown in Figure 3(e2), although the corresponding singlet and quintet states, panels (e1) and (e3), respectively, in Figure 3, have similar structures and nearly the same relative energies. Additional less stable isomers are shown in Figure S12.
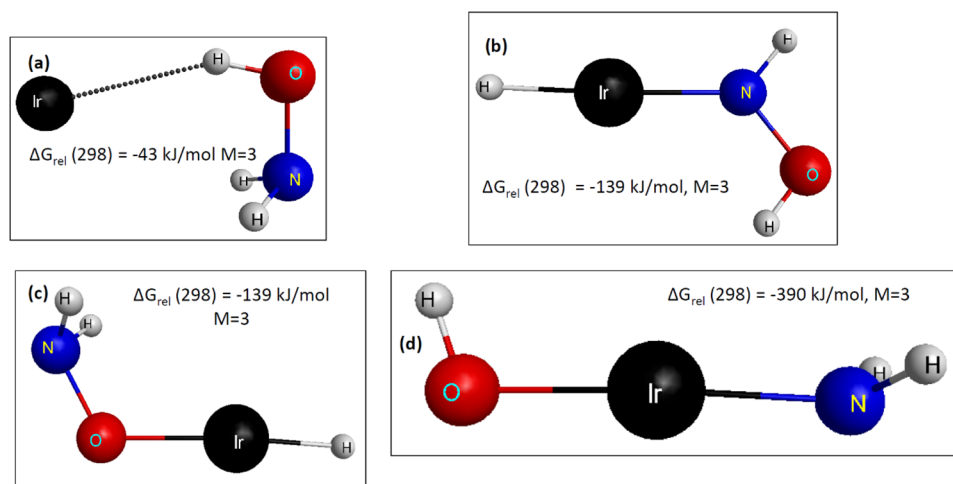
Figure 4. (a) Hydrogen-bonded complex between Ir^- and NH_2OH. (b) N−H fragmentation product. (c) O−H fragmentation product. (d) N−O fragmentation product. Free energies are at 298.15 K, relative to $Ir^- + NH_2OH$. M denotes the spin multiplicity.

3.4. Theoretical Vertical and Adiabatic Detachment Energies of $Ir_n(NOH)^-$ (n = 1−5). Vertical detachment energies (VDEs) and adiabatic detachment energies (ADEs) of the $Ir_n(NOH)^-$ (n = 1−5) anions were computed by using the lowest-energy structures shown in Figure 3. Single-point energy calculations of the corresponding neutral species were performed at the anion local minimum structures, taking the difference in electronic energies of neutral minus anion as the VDE. Multiple neutral spin states were calculated, with the smallest energy difference between neutral and anion taken as the theoretical VDE. For calculation of the ADEs, the neutral species were optimized, and the ADEs were computed as the difference in zero point energy-corrected electronic energies of the anion and neutral. For n = 1, the VDEs and ADEs of isomers (a1) and (a2) shown in Figure 3 were computed due to their nearly identical relative energies. The experimental VDEs and theoretical VDEs + ADEs of $Ir_n(NOH)^-$ (n = 1−5) are summarized in Table 1.

For n = 1, the calculated VDE and ADE for isomer $Ir(O)(NH)^-$, shown in Figure 3(a2), of 2.96 and 2.94 eV, respectively, are in excellent agreement with the measured value of 2.9 eV. In contrast, isomer $Ir(O)(N)(H)^-$ (Figure 3(a1)) has a calculated VDE (ADE) of 3.71 (3.47) eV, 0.8 (0.6) eV larger than the experimental value. This clearly suggests that isomer (a2) corresponds to the $Ir(NOH)^-$ species experimentally generated. For n = 2−5, the agreement between the measured and predicted VDEs is uniformly excellent, with differences of <0.1 eV. For n = 5, VDEs for the three isomers shown in Figure 3, (e1), (e2), and (e3), are similar, ranging from 3.32 to 3.41 eV, with isomers (e1) and (e2) showing slightly better agreement with the measured VDE of 3.3 eV. As noted previously, for n = 2−5 the VDEs are closer than the ADEs to the experimental data, suggesting that the measured peaks correspond to VDEs.

For comparison, the VDEs for some of the less stable isomers of $Ir_n(NOH)^-$ were also computed and are shown in Figures S9−S12. For n = 2 (Figure S9), predicted VDEs of 2.28 and 2.61 eV were obtained for two higher-energy isomers. This illustrates the sensitivity of the VDE to the isomer structure. Furthermore, the VDEs of the less stable isomers differ significantly from the observed VDE (3.02 eV), indicating that the less stable isomers are unlikely present in the experiments. Similar comments apply to n = 3−5 (Figures
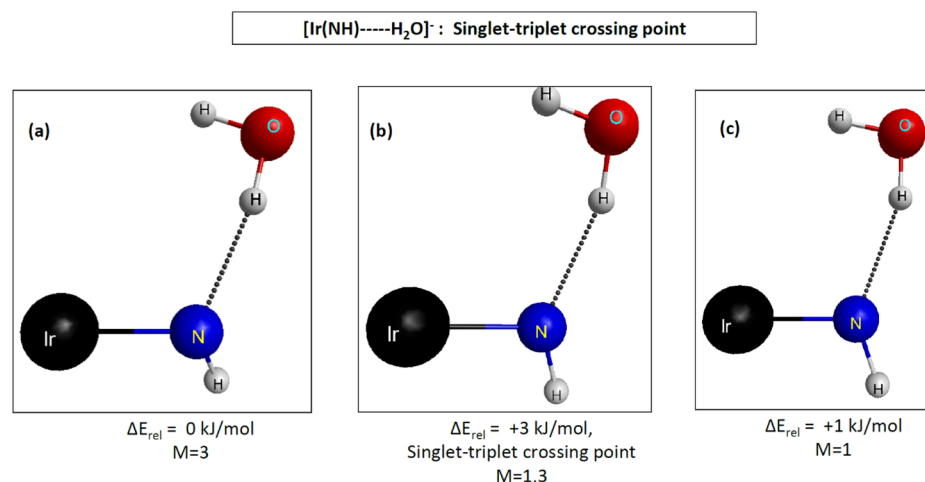
S10−S12), in which the predicted VDEs of the less stable isomers are in rather poor agreement with the corresponding measured VDEs and the predicted VDEs of the most stable isomers.

The VDEs of IrO_2^- and $Ir_2O_2^-$ were computed in a similar fashion, with values of 3.48 and 2.81 eV, respectively, and corresponding experimental values of 3.64 and 2.63 eV. While the differences between theory and experiment of 0.15−0.18 eV are somewhat larger than observed for the $Ir_n(NOH)^-$ series of anions, the level of agreement is nonetheless acceptable.

Electronic transition energies from the anion ground state species $Ir_n(NOH)^-$ (n = 1−4) to vertical excited states of the corresponding optimized neutral were computed by using time-dependent density functional theory (TDDFT) at the CAMQTP01/def2-TZVPP level, which are summarized in Table S1. For n = 1, a single excited state energy transition below the experimental measurement limit of 4.5 eV is predicted at 3.98 eV, which is 0.27 eV lower than the highest energy peak observed in the PES spectrum shown in Figure 2. For n = 2, there are three transition energies in the 3.6−4.3 eV range, all larger than the observed transitions between 2.5 and 3.5 eV in Figure 2. For n = 3, there is a predicted transition energy of 3.8 eV, which is near the measured transition energy at 3.9 eV. For n = 4, there are five predicted transition energies between 3.5 and 4.5 eV, all larger than the observed transitions in the 3.0−3.5 eV range.

As seen in Table S1, the number of electronic transitions below 4.5 eV grows rapidly with increasing number of iridium atoms. This is qualitatively consistent with the complexity of the observed PES spectra of the larger $Ir_n(NOH)^-$ species shown in Figure 2. Nonetheless, a more rigorous theoretical analysis which includes incorporation of Franck−Condon effects and consideration of vibronic transitions will be required to obtain further insights and interpretation of the measured spectra.

3.5. Formation of $Ir(NOH)^-$. As shown by the experimental data, a major product of the reactions between the anionic iridium clusters Ir_n^- and hydroxylamine is $Ir_n(NOH)^-$ accompanied by elimination of H_2; that is, $Ir_n^- + NH_2OH \rightarrow\rightarrow Ir_n(NOH)^- + H_2$. In principle, other reaction products are possible such as those listed below, with reaction free energies predicted at the ωB97x-d/def2 level of theory.

[Ir(NH)-----H₂O]⁻ : Singlet-triplet crossing point

(a) ΔE_{rel} = 0 kJ/mol, M=3

(b) ΔE_{rel} = +3 kJ/mol, Singlet-triplet crossing point, M=1,3

(c) ΔE_{rel} = +1 kJ/mol, M=1

Figure 5. $[Ir(NH)\cdots H_2O]^-$ structures at (a) the triplet state local minimum, (b) the singlet−triplet minimum energy crossing point, and (c) the singlet state local minimum. ΔE_{rel} denotes the relative electronic energies, and M denotes the spin multiplicity.
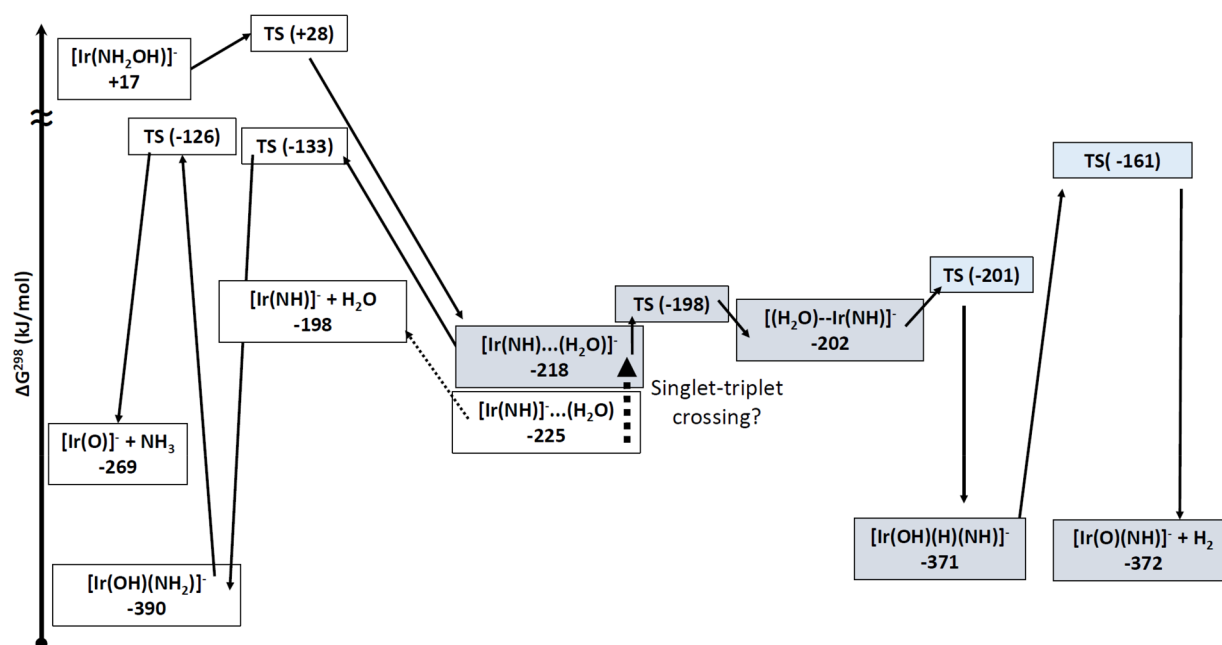
Figure 6. Potential energy diagram, not to scale, summarizing the key reaction steps leading to the formation of $Ir(O)(NH)^- + H_2$ and $Ir(O)^- + NH_3$. Free energies, in kJ/mol, are relative to $Ir^- + NH_2OH$. Unshaded boxes correspond to triplet states, whereas the blue-shaded boxes are singlet states.

$$Ir^- + NH_2OH \rightarrow Ir(H)(H)^- + HNO \quad \Delta G(298) = +17.1 \text{ kJ/mol} \tag{R2}$$

$$Ir^- + NH_2OH \rightarrow Ir(O)^- + NH_3 \quad \Delta G(298) = -268.6 \text{ kJ/mol} \tag{R3}$$

$$Ir^- + NH_2OH \rightarrow Ir(N)(H)^- + H_2O \quad \Delta G(298) = -270.3 \text{ kJ/mol} \tag{R4}$$

$$Ir^- + NH_2OH \rightarrow Ir(O)(NH)^- + H_2 \quad \Delta G(298) = -371.8 \text{ kJ/mol} \tag{R5}$$
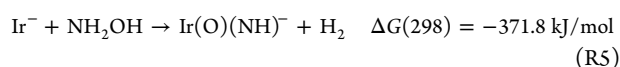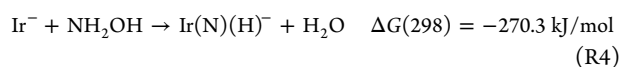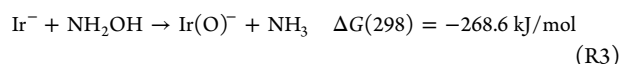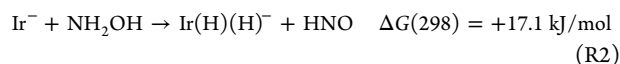
In reactions R2−R5, the predicted ground states of Ir^-, $Ir(O)^-$, and $Ir(H)(H)^-$ are triplets, whereas $Ir(O)(NH)^-$ and $Ir(N)(H)$ are singlets. Elimination of HNO is slightly endergonic, whereas eliminations of NH_3, H_2O, and H_2 are all exergonic processes. Because (R5) is the thermodynamically favored route and also corresponds to the primary reaction

products observed in the experiments, we focused our theoretical efforts on this particular reaction pathway.

To gain insights into the chemical processes leading to formation of $Ir_n(NOH)^- + H_2$, a detailed mapping of portions of the $Ir^- + NH_2OH$ potential energy surface was undertaken. In the following, all energies are relative to separated $Ir^-(^3X) + NH_2OH$. On the triplet surface, a hydrogen-bonded complex is formed between Ir^- and NH_2OH, with a free energy of −43 kJ/mol with respect to separated $Ir^- + NH_2OH$, as illustrated in Figure 4a. Additional less stable conformers are shown in Figure S13.

Initial fragmentation of NH_2OH can occur in three primary ways, via N−H, O−H, and N−O bond scission. The corresponding products of these three processes are $Ir(H)(NHOH)^-$, $Ir(H)(ONH_2)^-$, and $Ir(OH)(NH_2)^-$, which are shown in Figure 4, panels b, c, and d, respectively. The saddle point connecting the initial complex and the N−H

fragmentation product is shown in Figure S14, which has a barrier of 79 kJ/mol. Similarly, the saddle point for the O−H fragmentation process is shown in Figure S15, which has a smaller barrier of 56 kJ/mol.

Despite numerous attempts, on the triplet state surface we were unable to locate a saddle point directly connecting the initial complex and the N−O fragmentation product Ir(OH)-(NH$_2$)$^-$. However, starting from the slightly higher energy conformer of the Ir(NH$_2$OH)$^-$ complex identified in Figure S13e, a two-step reaction pathway leading to the N−O fragmentation product Ir(OH)(NH$_2$)$^-$ was identified, as shown in Figure S16. The first step of the reaction, with a barrier of 28 kJ/mol, involves concerted N−O bond dissociation and transfer of an H atom from NH$_2$ to OH, resulting in formation of H$_2$O which is hydrogen-bonded in the product to the thus-formed Ir(NH)$^-$ intermediate, with a relative energy of −225 kJ/mol. Because this barrier of 28 kJ/mol is smaller than that of both the N−H fragmentation process (79 kJ/mol, Figure S14) and the O−H fragmentation (56 kJ/mol, Figure S15), and hence more likely to play a key role in formation of the observed reaction products, this reaction pathway was studied in greater detail.

The next step of this reaction pathway involves concerted dissociation of an O−H bond with the H atom reattaching to the −NH fragment and the hydroxyl moiety attaching to Ir, resulting in formation of Ir(OH)(NH$_2$)$^-$ (Figure S16). However, it should be noted that on the triplet state surface simple breaking of the hydrogen bond in the Ir(NH)---H$_2$O$^-$ complex to produce separated Ir(NH)$^-$ and H$_2$O, at a relative energy of −198 kJ/mol, is energetically more favorable than crossing the second saddle point, which has a relative energy of −133 kJ/mol. However, a singlet−triplet minimum-energy crossing point in close structural and energetic proximity to the triplet state [Ir(NH)---H$_2$O]$^-$ complex was located and is shown in Figure 5 along with the singlet and triplet state local minima. The crossing point lies only 3 kJ/mol above the triplet local minimum, suggesting that crossover to the singlet state might readily occur. On the singlet surface, the [Ir(NH)---H$_2$O]$^-$ local minimum can undergo a simple internal migration of the water molecule, with the saddle point at a relative free energy of −198 kJ/mol, followed by a nearly barrier-free transfer of an H atom from water to the Ir atom to form Ir(OH)(NH)(H)$^-$, as illustrated in Figure S17. Finally, elimination of H$_2$ from Ir(OH)(NH)(H)$^-$ to form Ir(O)-(NH)$^-$ crosses a saddle point with a relative free energy of −161 kJ/mol, as shown in Figure S18. It should be noted that the final product, Ir(O)(NH)$^-$, shown in Figure 3(a2), is the isomer of Ir(NOH)$^-$ that has a predicted VDE (2.96 eV) in good agreement with the experimental value (2.9 eV), as discussed previously.

Figure 6 summarizes the key steps described above and shown individually in Figures S16−S18. Also shown on the left side of Figure 6 is a sequence of reaction steps, entirely on the triplet state surface, leading to formation of Ir(O)$^-$ + NH$_3$. However, this portion of the Ir$^-$ + NH$_2$OH potential energy surface is not discussed in detail since Ir(O)$^-$ is present even in the absence of hydroxylamine.

4. CONCLUSION

In this work, photoelectron spectra of mass-selected bare Ir$_n^-$ ($n = 1−5$) anionic clusters and Ir$_n$(NOH)$^-$ ($n = 1−5$) products were measured, and the photoelectron VDEs were found to be in excellent agreement with DFT calculations. The

reaction of Ir$^-$ with hydroxylamine to form Ir(NOH)$^-$ + H$_2$ is proposed to proceed through a triplet to singlet crossing and is exoergic by 372 kJ/mol. This pathway could help to explain the enhanced reactivity of hydroxylamine on iridium catalysts leading to large heat release and promoting ignition of HAN-based monopropellants. The systematic study of Ir$_n^-$ with hydroxylamine offers a wealth of information as to the fundamental reaction mechanisms common to these hetero-geneous catalytic reactions leading to combustion and ignition. Further expanding these studies to include more analogues of regularly employed fuels (hydrazines, nitrates, etc.) will give a better understanding as to the limitations of their current use in spacecraft thruster applications. This is critical in real-world applications for continued design and development of the next-generation fuels and catalysts, lowering the risks from exposure and explosive hazards and increasing the lifetime of the catalysts, thereby increasing the lifetime of the thrusters and spacecrafts as well.

■ ASSOCIATED CONTENT

ⓢ Supporting Information

The Supporting Information is available free of charge at https://pubs.acs.org/doi/10.1021/acs.jpca.1c03935.

> Details of additional experimental and theoretical results, including mass and photoelectron spectra, calculated representative isomers, and saddle point calculations (PDF)

■ AUTHOR INFORMATION

Corresponding Authors

Steven D. Chambreau − *Jacobs Technology, Inc., Air Force Research Laboratory, AFRL/RQRP, Edwards Air Force Base, California 93524, United States;* ⓞ orcid.org/0000-0003-2013-8376; Email: steven.chambreau.ctr@us.af.mil

Jerry A. Boatz − *Propellants Branch, Rocket Propulsion Division, Aerospace Systems Directorate, Air Force Research Laboratory, AFRL/RQRP, Edwards Air Force Base, California 93524, United States;* ⓞ orcid.org/0000-0002-7457-1610; Email: jerry.boatz@us.af.mil

Kit H. Bowen − *Department of Chemistry, Johns Hopkins University, Baltimore, Maryland 21218, United States;* ⓞ orcid.org/0000-0002-2858-6352; Email: kbowen@jhu.edu

Authors

Sandra M. Ciborowski − *Department of Chemistry, Johns Hopkins University, Baltimore, Maryland 21218, United States;* ⓞ orcid.org/0000-0001-9453-4764

Robert Buszek − *Jacobs Technology, Inc., Air Force Research Laboratory, AFRL/RQRP, Edwards Air Force Base, California 93524, United States*

Gaoxiang Liu − *Department of Chemistry, Johns Hopkins University, Baltimore, Maryland 21218, United States;* ⓞ orcid.org/0000-0002-1001-0064

Moritz Blankenhorn − *Department of Chemistry, Johns Hopkins University, Baltimore, Maryland 21218, United States*

Zhaoguo Zhu − *Department of Chemistry, Johns Hopkins University, Baltimore, Maryland 21218, United States;* ⓞ orcid.org/0000-0002-4395-9102

Mary A. Marshall − *Department of Chemistry, Johns Hopkins University, Baltimore, Maryland 21218, United States;* orcid.org/0000-0001-6614-1963

Rachel M. Harris − *Department of Chemistry, Johns Hopkins University, Baltimore, Maryland 21218, United States; Propellants Branch, Rocket Propulsion Division, Aerospace Systems Directorate and Jacobs Technology, Inc., Air Force Research Laboratory, AFRL/RQRP, Edwards Air Force Base, California 93524, United States; In-Space Propulsion Branch, Rocket Propulsion Division, Aerospace Systems Directorate, Air Force Research Laboratory, AFRL/RQRS, Edwards Air Force Base, California 93524, United States;* orcid.org/0000-0002-3585-5258

Tatsuya Chiba − *Department of Chemistry, Johns Hopkins University, Baltimore, Maryland 21218, United States*

Evan L. Collins − *Department of Chemistry, Johns Hopkins University, Baltimore, Maryland 21218, United States*

Sara Marquez − *Department of Chemistry, Johns Hopkins University, Baltimore, Maryland 21218, United States*

Ghanshyam L. Vaghjiani − *In-Space Propulsion Branch, Rocket Propulsion Division, Aerospace Systems Directorate, Air Force Research Laboratory, AFRL/RQRS, Edwards Air Force Base, California 93524, United States;* orcid.org/0000-0001-7473-7388

Complete contact information is available at:
https://pubs.acs.org/10.1021/acs.jpca.1c03935

Author Contributions

S.M.C., G.L., M.B., Z.Z., M.A.M., R.M.H., T.C, E.L.C., and S.M. completed the experimental photoelectron study. R.B., J.A.B., and S.D.C. performed the theoretical study. K.H.B., J.A.B., and S.D.C. conceived of and supervised the work.

Notes

The authors declare no competing financial interest.

■ REFERENCES

(1) Hwang, C. H.; Baek, S. W.; Cho, S. J. Experimental Investigation of Decomposition and Evaporation Characteristics of HAN-Based Monopropellants. *Combust. Flame* **2014**, *161*, 1109−1116.

(2) Amariei, D.; Courthéoux, L.; Rossignol, S.; Kappenstein, C. Catalytic and Thermal Decomposition of Ionic Liquid Monopropellants Using a Dynamic Reactor: Comparison of Powder and Sphere-Shaped Catalysts. *Chem. Eng. Process.* **2007**, *46*, 165−174.

(3) Amrousse, R.; Hori, K.; Fetimi, W.; Farhat, K. HAN and ADN as Liquid Ionic Monopropellants: Thermal and Catalytic Decomposition Processes. *Appl. Catal., B* **2012**, *127*, 121−128.

(4) Amrousse, R.; Katsumi, T.; Azuma, N.; Hori, K. Hydroxylammonium Nitrate (HAN)-Based Green Propellant as Alternative Energy Resource for Potential Hydrazine Substitution: From Lab Scale to Pilot Plant Scale-up. *Combust. Flame* **2017**, *176*, 334−348.

(5) Farshchi, M.; Vaezi, V.; Shaw, B. D. Studies of HAN-Based Monopropellant Droplet Combustion. *Combust. Sci. Technol.* **2002**, *174*, 71−97.

(6) Legge, R. S. L.; Lozano, P. C. Electrospray Propulsion Based on Emitters Microfabricated in Porous Metals. *J. Propul. Power* **2011**, *27*, 485−495.

(7) Schneider, S.; Hawkins, T.; Rosander, M.; Vaghjiani, G.; Chambreau, S.; Drake, G. Ionic Liquids as Hypergolic Fuels. *Energy Fuels* **2008**, *22*, 2871−2872.

(8) Chambreau, S. D.; Popolan-Vaida, D. M.; Vaghjiani, G. L.; Leone, S. R. Catalytic Decomposition of Hydroxylammonium Nitrate Ionic Liquid: Enhancement of NO Formation. *J. Phys. Chem. Lett.* **2017**, *8*, 2126−2130.

(9) Oxley, J. C.; Brower, K. R. In Thermal Decomposition Of Hydroxylamine Nitrate. *Proc. SPIE* **1988**, *0872*, 63−70.

(10) Lee, H. S.; Thynell, S. T. Confined Rapid Thermolysis/FTIR Spectroscopy of Hydroxylammonium Nitrate. In *33rd Joint Propulsion Conference and Exhibit*; American Institute of Aeronautics and Astronautics Inc.: 1997.

(11) Kidd, F. G.; Taylor, N. R.; Lemmer, K. M. Decomposition of Hydroxylammonium Nitrate in a Low Pressure Flowing Thermal Capillary System. *J. Mol. Liq.* **2018**, *262*, 396−404.

(12) Amrousse, R.; Katsumi, T.; Itouyama, N.; Azuma, N.; Kagawa, H.; Hatai, K.; Ikeda, H.; Hori, K. New HAN-Based Mixtures for Reaction Control System and Low Toxic Spacecraft Propulsion Subsystem: Thermal Decomposition and Possible Thruster Applications. *Combust. Flame* **2015**, *162*, 2686−2692.

(13) Hunt, L. B. A History of Iridium. *Platinum Metals Rev.* **1987**, *31*, 32−41.

(14) Foger, K.; Anderson, J. R. Hydrocarbon Reactions on Supported Iridium Catalysts. *J. Catal.* **1979**, *59*, 325−339.

(15) Vieira, R.; Bastos-Netto, D.; Ledoux, M.-J.; Pham-Huu, C. Hydrazine Decomposition over Iridium Supported on Carbon Nanofibers Composite for Space Applications: Near Actual Flight Conditions Tests. *Appl. Catal., A* **2005**, *279*, 35−40.

(16) Jiang, K.; Luo, M.; Peng, M.; Yu, Y.; Lu, Y.-R.; Chan, T.-S.; Liu, P.; de Groot, F. M. F.; Tan, Y. Dynamic Active-Site Generation of Atomic Iridium Stabilized on Nanoporous Metal Phosphides for Water Oxidation. *Nat. Commun.* **2020**, *11*, 2701.

(17) Pfeifer, V.; Jones, T. E.; Velasco Vélez, J. J.; Massué, C.; Greiner, M. T.; Arrigo, R.; Teschner, D.; Girgsdies, F.; Scherzer, M.; Allan, J.; et al. The Electronic Structure of Iridium Oxide Electrodes Active in Water Splitting. *Phys. Chem. Chem. Phys.* **2016**, *18*, 2292−2296.

(18) Rodrigues, J. A. J.; Cruz, G. M.; Bugli, G.; Boudart, M.; Djega-Mariadassou, G. Nitride and Carbide of Molybdenum and Tungsten as Substitutes of Iridium for the Catalysts used for Space Communication. *Catal. Lett.* **1997**, *45*, 1−3.

(19) Wu, W.-P.; Chen, Z.-F. Iridium Coating: Processes, Properties and Application. Part I. *Johnson Matthey Technol. Rev.* **2017**, *61*, 16−28.

(20) Wu, W.-P.; Chen, Z.-F. Iridium Coating: Processes, Properties and Application. Part II. *Johnson Matthey Technol. Rev.* **2017**, *61*, 93−110.

(21) Lee, S.; Fan, C.; Wu, T.; Anderson, S. L. Hydrazine Decomposition over Ir_n/Al_2O_3 Model Catalysts Prepared by Size-Selected Cluster Deposition. *J. Phys. Chem. B* **2005**, *109*, 381−388.

(22) Schmidt, M. W.; Gordon, M. S. The Decomposition of Hydrazine in the Gas Phase and over an Iridium Catalyst. *Z. Phys. Chem.* **2013**, *227*, 1301−1336.

(23) Castleman, A. W. Cluster Structure and Reactions: Gaining Insights into Catalytic Processes. *Catal. Lett.* **2011**, *141*, 1243−1253.

(24) Asmis, K. R.; Fielicke, A. Size-Selected Clusters as Model System for Catalysis. *Top. Catal.* **2018**, *61*, 1−2.

(25) Charles, E.; Sykes, H.; Christopher, P. Recent Advances in Single-Atom Catalysts and Single-Atom Alloys: Opportunities for Exploring the Uncharted Phase Space In-Between. *Curr. Opin. Chem. Eng.* **2020**, *29*, 67−73.

(26) Parkinson, G. S. Single-Atom Catalysis: How Structure Influences Catalytic Performance. *Catal. Lett.* **2019**, *149*, 1137−1146.

(27) Sweeny, B. C.; Ard, S. G.; Viggiano, A. A.; Shuman, N. S. Reaction of Mass-Selected, Thermalized $V_nO_m^+$ Clusters with CCl_4. *J. Phys. Chem. A* **2019**, *123*, 4817−4824.

(28) Ard, S. G.; Melko, J. J.; Ushakov, V. G.; Johnson, R.; Fournier, J. A.; Shuman, N. S.; Guo, H.; Troe, J.; Viggiano, A. A. Activation of Methane by FeO^+: Determining Reaction Pathways through Temperature-Dependent Kinetics and Statistical Modeling. *J. Phys. Chem. A* **2014**, *118*, 2029−2039.

(29) Sweeny, B. C.; Pan, H.; Ard, S. G.; Shuman, N. S.; Viggiano, A. A. On the Role of Hydrogen Atom Transfer (HAT) in Thermal Activation of Methane by MnO^+: Entropy vs. Energy. *Z. Phys. Chem.* **2019**, *233*, 771−783.

(30) Liu, G.; Ciborowski, S. M.; Zhu, Z.; Bowen, K. H. Activation of Hydroxylamine by Single Gold Atomic Anions. *Int. J. Mass Spectrom.* **2019**, *435*, 114−117.

(31) Liu, G.; Miliordos, E.; Ciborowski, S. M.; Tschurl, M.; Boesl, U.; Heiz, U.; Zhang, X.; Xantheas, S. S.; Bowen, K. Water Activation and Splitting by Single Metal-Atom Anions. *J. Chem. Phys.* **2018**, *149*, 221101.

(32) Liu, G.; Ciborowski, S. M.; Zhu, Z.; Chen, Y.; Zhang, X.; Bowen, K. H. The Metallo-Formate Anions, $M(CO_2)^-$, M = Ni, Pd, Pt, Formed by Electron-Induced CO_2 Activation. *Phys. Chem. Chem. Phys.* **2019**, *21*, 10955−10960.

(33) Liu, G.; Zhu, Z.; Ciborowski, S. M.; Ariyarathna, I. R.; Miliordos, E.; Bowen, K. H. Selective Activation of the C-H Bond in Methane by Single Platinum Atomic Anions. *Angew. Chem., Int. Ed.* **2019**, *58*, 7773−7777.

(34) Campbell, K. D.; Zhang, H.; Lunsford, J. H. Methane Activation by the Lanthanide Oxides. *J. Phys. Chem.* **1988**, *92*, 750−753.

(35) Van Koppen, P. A. M.; Kemper, P. R.; Bushnell, J. E.; Bowers, M. T. Methane Dehydrogenation by Ti^+: A Cluster-Assisted Mechanism for σ-Bond Activation. *J. Am. Chem. Soc.* **1995**, *117*, 2098−2099.

(36) Sun, G.; Zhao, Z.-J.; Mu, R.; Zha, S.; Li, L.; Chen, S.; Zang, K.; Luo, J.; Li, Z.; Purdy, C.; et al. Breaking the Scaling Relationship via Thermally Stable Pt/Cu Single Atom Alloys for Catalytic Dehydrogenation. *Nat. Commun.* **2018**, *9*, 4454.

(37) Du, J.; Sun, X.; Chen, J.; Jiang, G. A Theoretical Study on Small Iridium Clusters: Structural Evolution, Electronic and Magnetic Properties, and Reactivity Predictors. *J. Phys. Chem. A* **2010**, *114*, 12825−12833.

(38) Pawluk, T.; Hirata, Y.; Wang, L. Studies of Iridium Nanoparticles Using Density Functional Theory Calculations. *J. Phys. Chem. B* **2005**, *109*, 20817−20823.

(39) Davis, J. B. A.; Shayeghi, A.; Horswell, S. L.; Johnston, R. L. The Birmingham Parallel Genetic Algorithm and Its Application to the Direct DFT Global Optimisation of IrN (N = 10−20) Clusters. *Nanoscale* **2015**, *7*, 14032−14038.

(40) Zhang, W.; Xiao, L.; Hirata, Y.; Pawluk, T.; Wang, L. The Simple Cubic Structure of Ir Clusters and the Element Effect on Cluster Structures. *Chem. Phys. Lett.* **2004**, *383*, 67−71.

(41) Chen, M.; Dixon, D. A. Low-Lying Electronic States of Ir_n Clusters with n = 2−8 Predicted at the DFT, CASSCF, and CCSD(T) Levels. *J. Phys. Chem. A* **2013**, *117*, 3676−3688.

(42) Bussai, C.; Krüger, S.; Vayssilov, G. N.; Rösch, N. The Cluster Ir_4 and its Interaction with a Hydrogen Impurity. A Density Functional Study. *Phys. Chem. Chem. Phys.* **2005**, *7*, 2656−2663.

(43) Krüger, S.; Bussai, C.; Genest, A.; Rösch, N. Two Hydrogen Ligands on Tetrairidium Clusters: a Relativistic Density Functional Study. *Phys. Chem. Chem. Phys.* **2006**, *8*, 3391−3398.

(44) Balasubramanian, K.; Dai, D. Potential Energy Surfaces for Ir + H_2 and Ir^+ + H_2 Reactions. *J. Chem. Phys.* **1990**, *93*, 7243−7255.

(45) Castillo, S.; Bertin, V.; Solano-Reyes, E.; Luna-Garcia, H.; Cruz, A.; Poulain, E. Theoretical Studies on Hydrogen Activation by Iridium Dimers. *Int. J. Quantum Chem.* **1998**, *70*, 1029−1035.

(46) Feng, J.-N.; Huang, X.-R.; Li, Z.-S. A Theoretical Study on the Clusters Ir_n with n = 4, 6, 8, 10. *Chem. Phys. Lett.* **1997**, *276*, 334−338.

(47) Okumura, M.; Irie, Y.; Kitagawa, Y.; Fujitani, T.; Maeda, Y.; Kasai, T.; Yamaguchi, K. DFT Studies of Interaction of Ir Cluster with O_2, CO, and NO. *Catal. Today* **2006**, *111*, 311−315.

(48) Ge, Y.; Jiang, H.; Kato, R.; Gummagatta, P. Size and Site Dependence of the Catalytic Activity of Iridium Clusters toward Ethane Dehydrogenation. *J. Phys. Chem. A* **2016**, *120*, 9500−9508.

(49) Chen, Y.; Huo, M.; Chen, T.; Li, Q.; Sun, Z.; Song, L. The Properties of Ir_n(n = 2−10) Clusters and their Nucleation on c-Al_2O_3 and MgO Surfaces: from ab initio Studies. *Phys. Chem. Chem. Phys.* **2015**, *17*, 1680−1687.

(50) Qi, K.; Zhao, J.-M.; Wang, G.-C. A Density Functional Theory Study of Ethylene Hydrogenation on MgO-and γ-Al_2O_3-Supported Carbon-Containing Ir_4 Clusters. *Phys. Chem. Chem. Phys.* **2015**, *17*, 4899−4908.

(51) Ferrari, A. M.; Neyman, K. M.; Mayer, M.; Staufer, M.; Gates, B. C.; Rösch, N. Faujasite-Supported Ir_4 Clusters: A Density Functional Model Study of Metal-Zeolite Interactions. *J. Phys. Chem. B* **1999**, *103*, 5311−5319.

(52) Petrova, G. P.; Vayssilov, G. N.; Rösch, N. Density Functional Study of Hydrogen Adsorption on Tetrairidium Supported on Hydroxylated and Dehydroxylated Zeolite Surfaces. *J. Phys. Chem. C* **2007**, *111*, 14484−14492.

(53) Petrova, G. P.; Vayssilov, G. N.; Rösch, N. Hydrogen Adsorption on Zeolite-Supported Tetrairidium Clusters. Thermodynamic Modeling from Density Functional Calculations. *J. Phys. Chem. C* **2008**, *112*, 18572−18577.

(54) St. Petkov, P.; Petrova, G. P.; Vayssilov, G. N.; Rösch, N. Saturation of Small Supported Metal Clusters by Adsorbed Hydrogen. A Computational Study on Tetrahedral Models of Rh_4, Ir_4, and Pt_4. *J. Phys. Chem. C* **2010**, *114*, 8500−8506.

(55) Petrova, G. P.; Vayssilov, G. N.; Rösch, N. Density Functional Modeling of Reverse Hydrogen Spillover on Zeolite-Supported Tetrairidium Clusters. *Chem. Phys. Lett.* **2007**, *444*, 215−219.

(56) Vayssilov, G. N.; Rösch, N. Reverse Hydrogen Spillover in Supported Subnanosize Clusters of the Metals of Groups 8 to 11. A Computational Model Study. *Phys. Chem. Chem. Phys.* **2005**, *7*, 4019−4026.

(57) Shor, E. A. I.; Nasluzov, V. A.; Shor, A. M.; Vayssilov, G. N.; Rösch, N. Reverse Hydrogen Spillover onto Zeolite-Supported Metal Clusters: An Embedded Cluster Density Functional Study of Models M_6 (M = Rh, Ir, or Au). *J. Phys. Chem. C* **2007**, *111*, 12340−12351.

(58) Koyasu, K.; Tomihara, R.; Nagata, T.; Wu, J. W. J.; Nakano, M.; Ohshimo, K.; Misaizu, F.; Tsukuda, T. Sequential Growth of Iridium Cluster Anions based on Simple Cubic Packing. *Phys. Chem. Chem. Phys.* **2020**, *22*, 17842−17846.

(59) Lu, Y.; Zhao, J.; Tang, R.; Fu, X.; Ning, C. Measurement of Electron Affinity of Iridium Atom and Photoelectron Angular Distributions of Iridium Anion. *J. Chem. Phys.* **2020**, *152*, 034302.

(60) Davies, B. J.; Ingram, C. W.; Larson, D. J.; Ljungblad, U. The Electron Affinity of Iridium. *J. Chem. Phys.* **1997**, *106*, 5783−5784.

(61) Barysz, M.; Syrocki, Ł. Theoretical Interpretation of Photoelectron Spectra of the Iridium Neutral Atom and Anion. *J. Quant. Spectrosc. Radiat. Transfer* **2020**, *255*, 107278.

(62) Liu, G.; Ciborowski, S. M.; Bowen, K. H. Photoelectron Spectroscopic and Computational Study of Pyridine-Ligated Gold Cluster Anions. *J. Phys. Chem. A* **2017**, *121*, 5817−5822.

(63) Ho, J.; Ervin, K. M.; Lineberger, W. C. Photoelectron Spectroscopy of Metal Cluster Anions: Cu^-_n, Ag^-_n, and Au^-_n. *J. Chem. Phys.* **1990**, *93*, 6987.

(64) Chai, J.-D.; Head-Gordon, M. Systematic Optimization of Long-Range Corrected Hybrid Density Functionals. *J. Chem. Phys.* **2008**, *128*, 084106.

(65) Chai, J.-D.; Head-Gordon, M. Long-Range Corrected Hybrid Density Functionals with Damped Atom−Atom Dispersion Corrections. *Phys. Chem. Chem. Phys.* **2008**, *10*, 6615−6620.

(66) Weigend, F.; Ahlrichs, R. Balanced Basis Sets of Split Valence, Triple Zeta Valence and Quadruple Zeta Valence Quality for H to Rn: Design and Assessment of Accuracy. *Phys. Chem. Chem. Phys.* **2005**, *7*, 3297−3305.

(67) Rappoport, D.; Furche, F. Property-Optimized Gaussian Basis Sets for Molecular Response Calculations. *J. Chem. Phys.* **2010**, *133*, 134105.

(68) Andrae, D.; Häußermann, U.; Dolg, M.; Stoll, H.; Preuß, H. Energy-Adjusted ab initio Pseudopotentials for the Second and Third Row Transition Elements. *Theor. Chim. Acta* **1990**, *77*, 123−141.

(69) The def2-TZVPPD basis set and stuttgart pseudopotentials were downloaded from the Basis Set Exchange (BSE) website https://www.basissetexchange.org/.

(70) Pritchard, B. P.; Altarawy, D.; Didier, B.; Gibson, T. D.; Windus, T. L. A New Basis Set Exchange: An Open, Up-to-date Resource for the Molecular Sciences Community. *J. Chem. Inf. Model.* **2019**, *59*, 4814−4820.

(71) Feller, D. The Role of Databases in Support of Computational Chemistry Calculations. *J. Comput. Chem.* **1996**, *17*, 1571−1586.

(72) Schuchardt, K. L.; Didier, B. T.; Elsethagen, T.; Sun, L.; Gurumoorthi, V.; Chase, J.; Li, J.; Windus, T. L. Basis Set Exchange: A Community Database for Computational Sciences. *J. Chem. Inf. Model.* **2007**, *47*, 1045−1052.

(73) Ishida, K.; Morokuma, K.; Komornicki, A. The Intrinsic Reaction Coordinate. An ab initio Calculation for HNC-HCN and H⁻ + CH₄-CH₄+H⁻. *J. Chem. Phys.* **1977**, *66*, 2153−2156.

(74) Gonzalez, C.; Schlegel, H. B. An Improved Algorithm for Reaction Path Following. *J. Chem. Phys.* **1989**, *90*, 2154−2161.

(75) McQuarrie, D. A. *Statistical Mechanics*; Harper & Row: New York, 1975.

(76) The zero point energy scale factor of 0.975 used here is the value recommended for ωB97x-d/def2-TZVP. See: Alecu, I. M.; Zheng, J.; Zhao, Y.; Truhlar, D. G. Computational Thermochemistry: Scale Factor Databases and Scale Factors for Vibrational Frequencies Obtained from Electronic Model Chemistries. *J. Chem. Theory Comput.* **2010**, *6* (9), 2872−2887.

(77) Jin, Y.; Bartlett, R. J. The QTP Family of Consistent Functionals and Potentials in Kohn-Sham Density Functional Theory. *J. Chem. Phys.* **2016**, *145* (3), 034107.

(78) Schmidt, M. W.; Baldridge, K. K.; Boatz, J. A.; Elbert, S. T.; Gordon, M. S.; Jensen, J. H.; Koseki, S.; Matsunaga, N.; Nguyen, K. A.; Su, S. J.; et al. General Atomic and Molecular Electronic Structure System. *J. Comput. Chem.* **1993**, *14*, 1347−1363.

(79) Gordon, M. S.; Schmidt, M. W. Advances in Electronic Structure Theory: GAMESS a Decade Later. In *Theory and Applications of Computational Chemistry*; Elsevier: 2005; pp 1167−1189.

(80) Gozem, S.; Krylov, A. I. The EzSpectra Suite: An Easy-to-use Toolkit for Spectroscopy Modeling. *Wiley Interdiscip. Rev.: Comput. Mol. Sci.* **2021**, No. e1546.